

New universality classes and BKT transition in the vortex lattice phases of Kagome Ice

Wei Zhang,¹ Wanzhou Zhang,^{1,*} Jie Zhang,¹ Chengxiang Ding,^{2,†} and Youjin Deng^{3,4,‡}

¹*College of Physics and Optoelectronics, Taiyuan University of Technology, Shanxi 030024, China*

²*School of Science and Engineering of Mathematics and Physics,
Anhui University of Technology, Maanshan, Anhui 243002, China*

³*Hefei National Laboratory for Physical Sciences at the Microscale and Department of Modern Physics,
University of Science and Technology of China, Hefei 230026, China*

⁴*Hefei National Laboratory, University of Science and Technology of China, Hefei 230088, China*

(Dated: June 3, 2025)

Inspired by the experimental realization of direct Kagome spin ice [Nature Nanotechnology 19, 1101–1107 (2024)], the theoretical six-vertex model on the Kagome lattice is systematically simulated using the directed loop Monte Carlo method. Four distinct vortex lattice phases are identified: (i) Ferromagnetic leg states and vortex lattice order on both triangular and honeycomb faces, with a winding number $k = 1$. (ii) Antiferromagnetic leg states and vortex lattice order on both types of faces, with $k = -2$ on the honeycomb faces and $k = 1$ on the triangular faces. (iii) Paramagnetic leg states and vortex lattice order on the triangular faces with $k = 1$. (iv) Paramagnetic leg states and vortex lattice order on the honeycomb faces with $k = 1$. As for ferromagnetic to different types of magnetic disorder phase, besides the Ising universality class with $y_t = 1$, a new critical exponent $y_t = 1.317(6)$ has also been found. The transition between the third and fourth types of vortex lattice phases occurs with the new exponent $y_t = 1.340(3)$. The third and fourth types of the vortex lattice phase to the vortex disorder phase are found to be of the Berezinskii-Kosterlitz-Thouless type. These findings contribute to the search for and understanding of ice on complex lattices.

I. INTRODUCTION

Ice is a substance commonly found in nature and is a fascinating subject for studying various types of phase transitions. There are several distinct forms of ice, such as the water ice [1], spin ice observed in natural materials [2], artificial spin ice [3, 4], and particle-based ice [5]. A key characteristic shared by all these types of ice is the “ice rule”, i.e., the two-in (close) two-out (far away) constraint [6].

Water ice exhibits 19 stable geometric structures, currently identified through high-pressure and low temperature experiments [1]. There are also bilayer water ice experimentally grown on a Au(111) surface [7, 8]. Additionally, artificial spin ices [9] are also created, typically using magnetically interacting nanoislands or nanowire links [10], superconducting-qubit arrays [11] and so on. The colloidal particle-based ice [12], is another artificial system capable of realizing various ices. The colloidal particle ices employ elongated optical traps to confine the colloidal particles. Each optical trap features two wells where the colloidal particles can reside. These arrays of traps can organize into different kinds of lattices [5, 12–16]. Experimentally, the ice model can also be realized by confining colloidal active fluids in microchannel networks [17, 18].

In the ice naturally formed in nature or created artificially, the Kagome lattice ice, due to its geometric

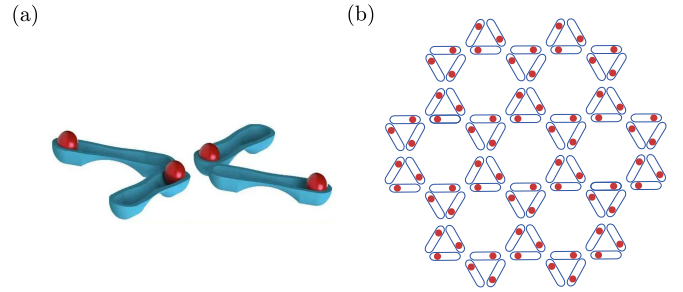


Figure 1. The colloidal particle-based ice (a) employs elongated optical traps to confine colloidal particles (b) in an ASI configuration on a Kagome lattice.

frustration [19], has become a popular lattice for studying artificial ice. The traditional Kagome artificial spin ice (ASI) was constructed by placing nanomagnets on the edges of a honeycomb lattice. In contrast, in 2024, direct experimental realization of Kagome artificial ice was achieved [20], where the nanomagnets are placed on the edges of a Kagome lattice. The configurations of the nanomagnets can be described by the well-known 16 vertex model. However, the physics of the six-vertex (6V) model remains unclear from the perspective of numerical simulations.

Using the 6V model, the possible vortex lattice (VL) phases [21] and their transition are interesting topics. In certain geometric lattices, such as the bilayer honeycomb lattice [7, 8], the melting of the VL into a disordered phase occurs via a first-order transition. Similar behavior has been observed in real materials such as YBCO and $\text{YBa}_2\text{Cu}_3\text{O}_7$ [22–25]. However, on the simple square

* zhangwanzhou@tyut.edu.cn

† dingcx@ahut.edu.cn

‡ yjdeng@ustc.edu.cn

lattice, the 6V model exhibits a BKT transition [26]. This can be understood. From duality arguments and mapping to Coulomb gas systems, the 6V model, with special parameters, is known to be asymptotically equivalent to the two-dimensional XY model at criticality [26]. In the XY model, the unbinding of vortex-antivortex pairs is considered as the cause of the BKT phase transition [27, 28].

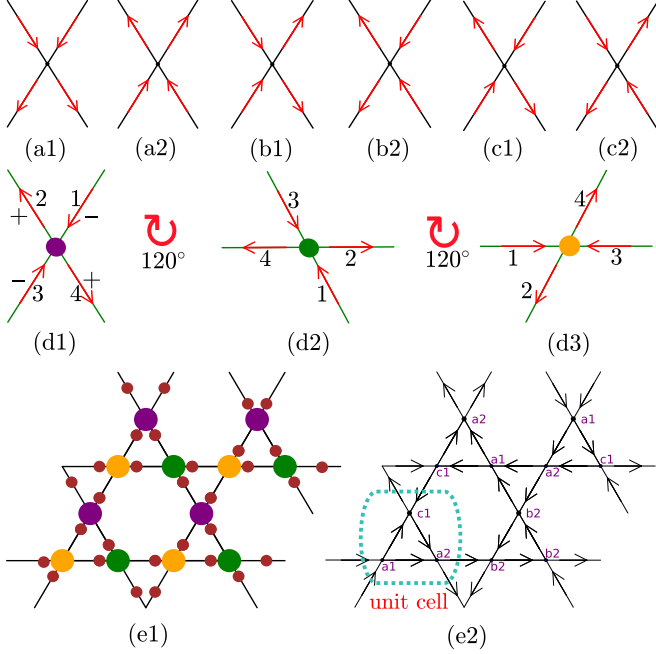


Figure 2. Configuration of 6V model. (a1)-(c2) show six types of vertices and their leg configurations; (d1)-(d3) show three types of vertex positions and their leg labels; (e1) shows a possible water ice configuration; (e2) shows 2×2 vertex configurations. The unit cells have three vertices and an upright triangular shape Δ .

A question emerges: *Are there interesting vortex lattice phases in the Kagome lattice for the ice model, and what types of transition occur between them?*

To explore this question, we systematically simulate the 6V model on the Kagome lattice using the directed-loop Monte Carlo method [29–32]. The overall phase diagram is obtained from the order parameters related with magnetic moments and vortices. In the phase diagram, the antiferromagnetic phase coincides with the VL-I phase, and the ferromagnetic phase coincides with the VL-II phase. In the magnetically disordered phase, we observe two another VL phases. Because the vortices exist on triangular and honeycomb faces, the phases are defined as the VL-T and VL-H phases, respectively, where T and H are the initials of “triangle” and “honeycomb”.

The details of the phase transitions are also studied carefully. Two distinct critical exponents are obtained for the transition from ferromagnetic to two types of disordered phases: the Ising universality class $y_t = 1$ (to

VL-T) and a new universality class $y_t = 1.317(6)$ (to VL-disorder). Furthermore, two of the vortex lattice phases (VL-T and VL-H) melt into disorder phase via BKT type of transition. The transition between the VL-H and VL-T phases occurs with the exponent $y_t = 1.340(3)$. Experimentally, it could be realized by colloidal particles and traps arrays in a Kagome lattice shape, as shown in Fig. 1.

The outline of this work is as follows. Sec. II introduces the 6V model on the Kagome lattice, the directed loop algorithm, and the main measured quantities. Sec. III A shows the global phase diagram by the magnetic moments. New exponents are found from the ferromagnetic phase to the disorder phase. Sec. III B describes the global phase diagram by vortex. Conclusive comments and outlook are made in Sec. IV. In the appendix A and B, we confirm our code by the enumeration method and the worm method.

II. MODELS, AND OBSERVED QUANTITIES

A. The short review of the 6V Model

Since the ice rule was introduced in 1935 [33], the 6V model has been extensively studied. In 1967, Lieb [34] calculated the free energy per site exactly. The 6V model is exactly solvable. Over time, the 6V model has seen several generalizations, such as the 8V, 16V, 19V, and 32V models [35]. It can be mapped to other statistical models, including the Ising model [36], the Potts model [37], and the Ashkin-Teller model [38]. The 6V model can also be mapped to the quantum XXZ chain by taking an anisotropic limit [39]. For a comprehensive theoretical review of earlier works, refer to the book by Baxter [40] (1982) and a detailed review of the integrability of the 6V model [41].

As for the 6V model on the Kagome lattice, Baxter (1978) demonstrated that the triangular Potts model is equivalent to the restricted Kagome 6V model [42]. B. Nienhuis (1982) established that the restricted Kagome 6V model is equivalent to the $O(n)$ model on the honeycomb lattice, and to the Potts model on the triangular lattice [43].

B. The 6V Model

Figure 2 (a) presents six typical configurations of the 6V model on the Kagome lattice, which satisfy the condition of two incoming and two outgoing. Based on the states of the legs, the type of each vertex can be determined and is represented by the symbols a1-c2. Compared with the vertices in the shape of a “+” on the square lattice, the legs pointing upwards, downwards, to the left, and to the right on the square lattice correspond to the legs numbered 1, 3, 2, and 4 of the Kagome lattice, as shown in Fig 2 (b).

The six vertices have their own weights W_i as $a1, a2, b1, b2, c1, c2$, respectively. In this work, for simplicity, we set $a1 = a2, b1 = b2$, and $c1 = c2$. According to the Boltzmann distribution, the vertices also have their energy defined as

$$\varepsilon_i = -\frac{\ln W_i}{\beta}, \quad i = 1, \dots, 6 \quad (1)$$

where β is the inverse temperature.

As shown in Fig. 2 (d1), in mathematical notation, we represent the state of the arrow pointing towards the vertex as a “+” sign, and the state of the arrow pointing away from the vertex as a “-” sign. Considering that in the Kagome lattice, in addition to the upright paired opposite triangles ∇ and \triangle , there are also tilted paired opposite triangles ∇ and \triangle . Since the states of the legs at the vertex are closely related to the weight and energy of the vertex, it is necessary to number the legs after strictly tilting them. As shown in Figs. 2 (d1)-(d3), ∇ can be obtained by rotating \triangle clockwise by 120 degrees, and \triangle can be obtained by rotating ∇ clockwise by another 120 degrees. During the rotation process, the numbering of the legs is bounded to the legs themselves. This type of definition was introduced in 1982 [43].

Our theoretical ice model can also inspire first-principles calculations [44] to explore the water ice model on the Kagome lattice. As shown in Figs. 2 (e1) and (e2), when H^- moves away from O^{-2} , an arrow pointing away from the vertex is used to represent it. When H^- moves toward O^{-2} , an arrow is used pointing towards the vertex. Figure 2 (e2) shows typical vertex configurations with 2×2 unit cells, and each unit cell has three vertices.

C. Directed loop algorithm

In this paper, we apply the directed loop algorithm [30–32], which has been used to simulate the single-layer [29] ice and the bilayer-ice model [45]. A similar loop algorithm is the worm algorithm [46, 47] with very efficient dynamical behaviours [48]. The 6V model is similar to the flow representation of other models [49–51], suitable for simulation using the loop types of algorithm. In the directed loop, one MC step contains several loop updates. As shown in Fig. 3, first, randomly select a vertex, and then randomly choose one of the legs, as indicated by the position marked as “begin” or loop head. When the loop head enters the leg corresponding to the vertex, it is called the entrance leg. The leg from which the loop head exits the vertex is called the exit leg. Then, let the loop head move randomly in space, with the probability of the walking direction designed to prevent bouncing. There are two ways for the loop head to close, as shown in Figs. 3 (a) and (b). The loop closes when the exit leg links to the beginning leg. The other way is when the exit leg exactly coincides with the beginning leg.

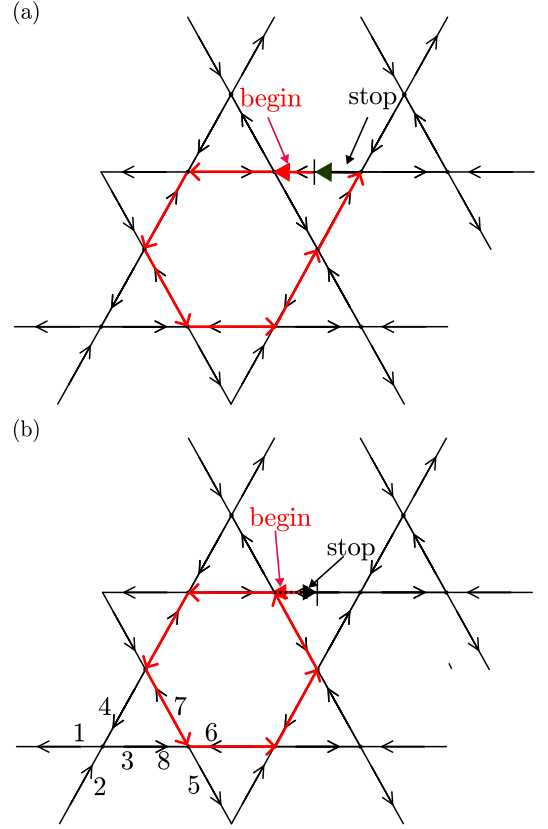


Figure 3. Two types of loop close methods. If one type of loop closure is missing, it will result in longer loops, causing the code to slow down. Similar to the process in quantum Monte Carlo simulations, a linked list is also constructed. For instance, leg 3 and leg 8 are interlinked with each other.

The probabilities for the various exit legs, given a specific vertex type and an entrance leg, are selected to ensure that the detailed balance condition holds. This results in directed-loop equations. In the solutions, if the bounce probabilities can be avoided, the algorithm’s efficiency will be high.

Here, a detailed process of constructing the system of equations is provided for easier follow-up. For convenience, we label the 6V types in Fig 2 (a) as 1 to 6. Suppose we encounter the vertex type 6, and assume that we are entering from leg 3. Then, we attempt to exit from the legs 1, 2, 3, and 4 in sequence. During this process, if leg 1 is used as the exit leg, it results in the formation of a non-existent vertex. As a result, only three valid vertices (2, 6, and 3) can exist. Therefore, the exit legs are 2, 3, and 4 with the entrance leg marked 3, respectively. Using these three vertices, arranged in the order 2, 6, and 3, placed in the top row and the left column as shown in Fig 4 (a), the transition weights between these vertices correspond to the variables in the 3×3 system of equations. The matrix element $a_{(i,j)}$ represents the weight associated with the transition from type i to type j . For the first row, for example, $a_{(2,2)}$, $a_{(2,6)}$, and $a_{(2,3)}$ represent the transition weights from vertex type 2 to vertices

2, 6, and 3, respectively. The corresponding entry leg is fixed at 2, because the transition from vertex 6 to vertex 2 enters via leg 3, but exits via leg 2. Similarly, for the second (third) row, the transitions from vertex 6 (3) to the other vertices have the entry leg fixed at 3 (4). The sum of the elements in each row of a equals the weights of the corresponding reference vertices W_2 , W_6 and W_3 .

Refs. [29–32] provide the solutions of bounce-free systems of equations. However, the condition requires $W_2 > W_6 > W_3$, but in reality, it is possible that our situation is $W_6 > W_2 > W_3$. Therefore, by swapping the first two rows and the first two columns of Fig 4 (a), a new system of equations can be obtained, as shown in Fig 4 (b).

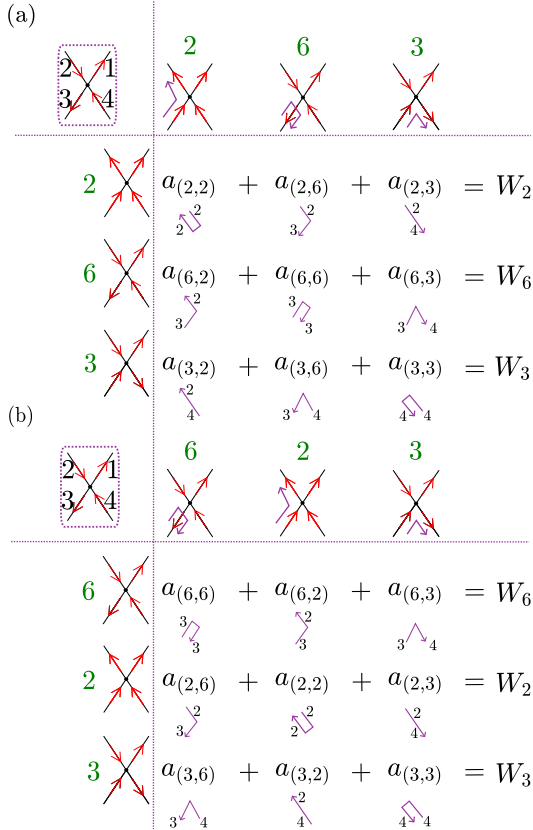


Figure 4. Equation groups of the directed loop probabilities $a_{i,j}$ (a) before sorting of the vertex weight W_i , $i = 2, 3, 6$ and (b) after sorting.

To solve for the elements in Fig. 4(b), for convenience, the positions of the matrix elements are marked with superscripts, for example, $a^{(1,1)} = a^{(6,6)}$ and $W^{(1)} = W_6$. If $W^{(1)} \leq W^{(2)} + W^{(3)}$, a set of bounce-free solutions is defined as follows:

$$\begin{aligned} a^{(1,2)} &= \frac{W^{(1)} + W^{(2)} - W^{(3)}}{2} \\ a^{(1,3)} &= \frac{W^{(1)} - W^{(2)} + W^{(3)}}{2} \\ a^{(2,3)} &= \frac{-W^{(1)} + W^{(2)} + W^{(3)}}{2} \end{aligned} \quad (2)$$

If $W^{(1)} > W^{(2)} + W^{(3)}$, a bounce solution needs to be introduced as

$$\begin{aligned} a^{(1,1)} &= W^{(1)} - W^{(2)} - W^{(3)} \\ a^{(1,2)} &= W^{(2)} \\ a^{(2,3)} &= W^{(3)} \end{aligned} \quad (3)$$

Then, we normalize these matrix elements, and the normalization formula is as follows:

$$p^{(i,j)} = \frac{a^{(i,j)}}{W^{(i)}} (j = 1, 2, 3) \quad (4)$$

The outgoing leg is determined based on a random number as follows:

- If $0 \leq \text{rand}() < p_1$, the outgoing leg is the 1st possible leg that has a chance to exit, though its actual number may be 1 or 2.
- If $p_1 \leq \text{rand}() < p_2$, the outgoing leg is the 2nd possible leg that has a chance to exit
- If $p_2 \leq \text{rand}() < 1$, the 3rd possible leg that has a chance to exit

The above process determines the outgoing leg in the loop constructing.

D. The observable quantities

In order to better characterize the phases and phase transitions of the Kagome lattice, the following quantities are introduced.

1. specific heat, magnetic moment, Binder ratio and susceptibility

- Specific heat

$$C_V = \frac{1}{NT^2} \left(\langle E^2 \rangle - \langle E \rangle^2 \right) \quad (5)$$

Here T denotes temperature, and $\langle \rangle$ denotes averaging. The energy of the system E :

$$E = \sum_{i=1}^N \varepsilon_i \quad (6)$$

where ε_i is the energy corresponding to each vertex and N denotes the total number of vertices.

- Ferromagnetic moment along the x direction

$$M_F = \frac{1}{N} \left\langle \left| \sum_{i=1}^N S_{i,x} \right| \right\rangle, \quad (7)$$

$S_{i,x}$ is the state of the leg in the x direction for the vertex i . The values of $S_{i,x}$ can be +1 or -1. After testing, the magnetic moments along the other two directions of the triangle's edges are equivalent to the x - direction and do not need to be measured.

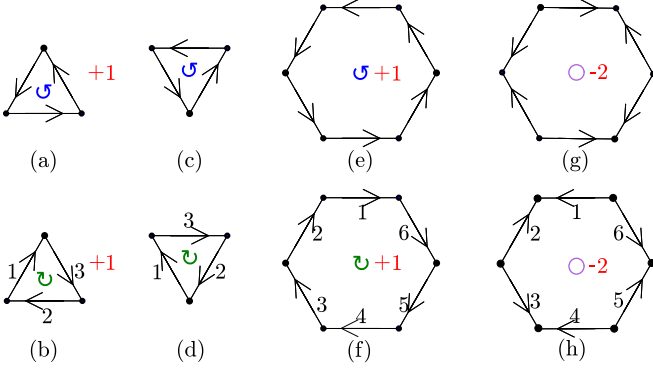


Figure 5. The vortex configurations on the triangular and hexagonal faces are marked with the winding number k in red numbers beside them, and the rotation direction is indicated by colored arrows. (a)-(d) $k = 1$, (e)-(f) $k = 1$, (g)-(h) $k = -2$.

- Antiferromagnetic moment along the x direction

$$M_A = \frac{1}{N} \left\langle \left| \sum_{i=1}^N (-1)^{i_x} S_{i,x} \right| \right\rangle, \quad (8)$$

where i_x is the index of the i -th vertex along the horizontal direction, or the column index, in the Kagome lattice.

- Binder ratio corresponding to the magnetic moment

$$Q = \frac{\langle M^2 \rangle^2}{\langle M^4 \rangle} \quad (9)$$

Here M can be taken as the ordinal parameter M_A , M_F above.

- Magnetic susceptibility,

$$\chi = \frac{1}{NT^2} \left(\langle M^2 \rangle - \langle M \rangle^2 \right) \quad (10)$$

2. vortex and winding number

The states of the legs in the Kagome lattice, within the triangular and hexagonal faces, also form interesting VL phases. To distinguish between different vortex-related phases, the concept of vorticity is used here,

$$\oint_c \nabla \theta \cdot d\mathbf{l} = 2\pi k, \quad k = \pm 1, \pm 2, \dots, \quad (11)$$

the term $\oint_c \nabla \theta \cdot d\mathbf{l}$ is the line integral along the closed path c , which calculates the total angular change around the vortex. The result of the integral is $2\pi k$, where k is the winding number.

In Figs. 5 (a)-(d), the vortex configurations on the triangular faces are shown. The blue represents a counterclockwise vortex and the green represents a clockwise vortex, but both have a winding number $k = 1$.

In Figs. 5 (e)-(f), the vortex configurations on the honeycomb faces are shown. Both have a winding number $k = 1$. However, as shown in Figs. 5 (g)-(h), both have a winding number $k = -2$.

To further illustrate this, we can consider the angular differences in various geometric configurations to show the characteristics of the vortex. The following three equations describe the sum of the angular differences in triangular and honeycomb faces:

$$\triangle : \sum_{i=1}^3 \theta_{\text{mod}(i,3)+1} - \theta_i = 2\pi, \quad (12a)$$

$$\text{hexagon} : \sum_{i=1}^6 \theta_{\text{mod}(i,6)+1} - \theta_i = 2\pi, \quad (12b)$$

$$\text{hexagon} : \sum_{i=1}^6 \theta_{\text{mod}(i,6)+1} - \theta_i = -4\pi. \quad (12c)$$

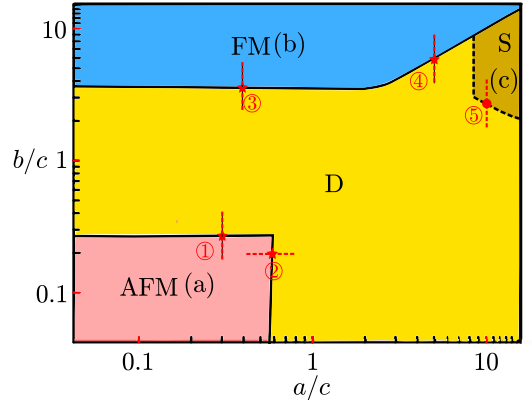


Figure 6. The schematic representation of the different magnetic phases, including the FM, AFM, disorder (D), and striped (S) region. The lines serve as a guide for the eyes, and the points are obtained from finite size scaling. For convenience, the labels (a)-(c) are used to mark the positions of the parameters taken for the snapshots drawn later in the phase diagram.

III. RESULTS

This model can obtain a phase diagram through the magnetic moment and another phase diagram through vortices. To simplify, we will discuss them separately.

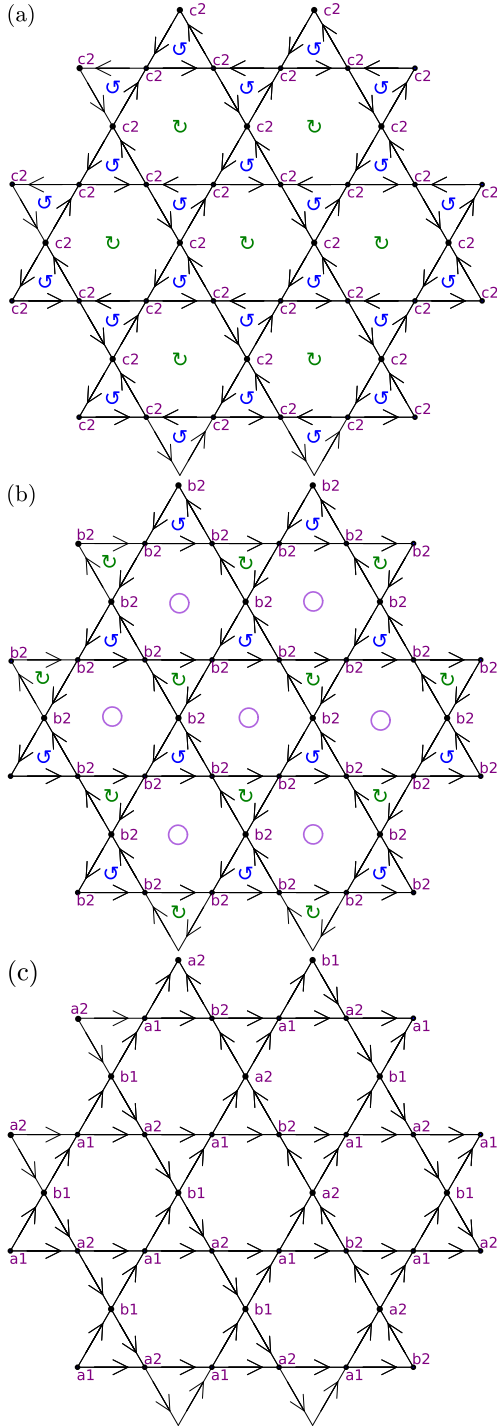


Figure 7. Snapshot of (a) AFM phase with winding number $k_T = 1$ and $k_H = 1$. (b) FM phase with $k_T = 1$ and $k_H = -2$ (c) Striped (S) region with $k_T = k_H = 0$.

A. Global phase diagram by magnetic moments

1. Phase diagram and typical snapshots

Figure 6 shows the global phase diagram, which contains the anti-ferromagnetic (AFM), ferromagnetic (FM), and disordered (D) phase. The phase diagram is plotted in the $a/c - b/c$ plane. In the actual simulation process, we define the weight of the c -type vertex as a constant 1, and adjust the ratio of $\frac{a}{c}$ and $\frac{b}{c}$ between 0.1 and 10.

The AF phase occurs in the region where both a and b are smaller than c , marked by the light red region, meaning that in this case, the $c2$ -type vertices occupy the entire lattice, as shown in Fig. 7 (a).

The FM phase occurs in the region where b are larger than a and c , marked by the blue region, which means that in this case, the $b2$ -type vertices occupy the entire lattice, as shown in Fig. 7 (b).

In Fig. 7 (c), the striped region (disorder phase) occurs in the place where both a and b are larger than c , as indicated by the brown color. In the x -direction, every leg is in the same state, with each leg pointing either left or right. However, the directions of the arrows between each row are random, and we refer to this as an x -striped region, although it still represents a disordered phase.

This phase diagram is completely different from that of the square lattice. The phase diagram of the square lattice is symmetric with respect to $a = b$, where either a or b being very large can form a ferromagnetic phase. However, in the Kagome lattice, the symmetry is broken. For example, when b is very large, the b -type vertices can fully occupy the Kagome lattice, forming a ferromagnetic phase. However, when a is very large, the a -type vertices cannot fully occupy the entire lattice, preventing the formation of a ferromagnetic phase.

2. Ising universality $y_t = 1$ at $a = 0.3$

To explore the nature of the AFM-D phase transition, the physical quantities Q and susceptibility χ are simulated near the phase transition point, as shown in cut ① in Fig. 6.

In Fig. 8 (a), when $a = 0.3$, Q is shown for $L = 10, 16, 22, 28, 36, 42$ as b is scanned along the cut. To analyze the data near the critical point b_c , finite-size scaling is performed using the following equation:

$$Q = Q_0 + e_1(b - b_c)L^{y_t} + e_2(b - b_c)^2L^{2y_t} + f_1L^{-w}, \quad (13)$$

where y_t is the thermal exponent, and e_1, e_2, f_1 are non-universal expansion coefficients and w is fixed to 1. The fitting using the least-squares method gives $b_c = 0.268(1)$. The critical exponent is $y_t = 1.01(2)$ indicating the Ising universality. Based on the estimated precise phase transition point and critical exponents, we

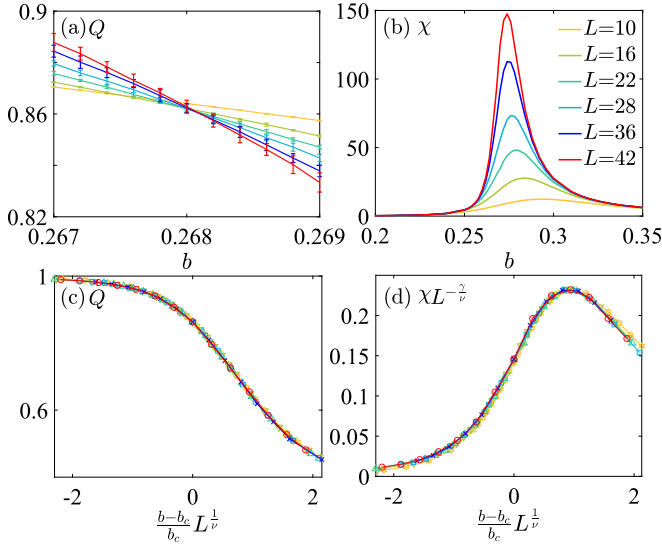


Figure 8. The details along the cut ④ (a) Q versus b (b) χ (c) data collapse of Q (d) data collapse of χ . The exponents $y_t = 1$ indicates the phase transition belongs to the Ising transition.

also perform data collapse, where the horizontal axis represents tL^{y_t} and the vertical axis represents Q , where t is the reduced parameter defined as $\frac{b-b_c}{b_c}$. The Q curves from the different sizes collapse nicely onto each other, as shown in Fig. 8 (c).

To calculate the critical exponent γ , the following scaling hypothesis formula is used,

$$\chi_{max} \propto |t|^{-\gamma} \propto L^{\gamma/\nu}. \quad (14)$$

Taking the logarithm of both sides of the above formula, the corresponding slope is the exponent γ/ν , and its fitted value is 1.76(1), which is consistent with the Ising exponent $\gamma = 7/4 = 1.75$ within the errorbar.

Using the evaluated exponent γ , we also perform data collapse by plotting $\chi L^{-\gamma/\nu}$ versus $tL^{1/\nu}$, where the curves for different system sizes overlap very well [52]. Using the following scaling relations,

$$\alpha + 2\beta + \gamma = 2, \quad (15a)$$

$$\gamma = \beta(\delta - 1), \quad (15b)$$

$$\nu d = 2 - \alpha, \quad (15c)$$

$$\gamma = \nu(2 - \eta), \quad (15d)$$

the remaining exponents $\alpha \approx 0$, $\delta \approx 15$, $\eta \approx \frac{1}{4}$, and $\beta \approx 0.125$. These critical exponents are consistent with Ising universality.

3. New universality and exponent $y_t = 1.317(6)$ at $a = 5$

As the parameter b changes from $b = 0.3$ to $b = 0.5$, the critical exponent changes, even though the phase transition is fixed from the ferromagnetic (FM) to magnetic disorder(D) regions.

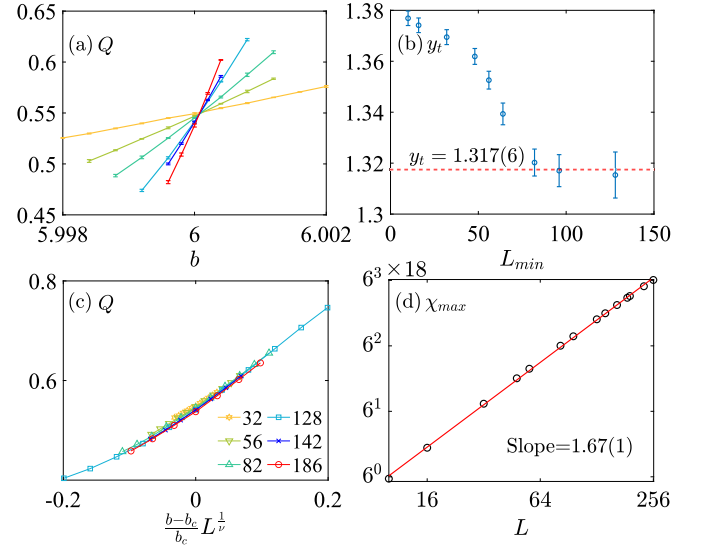


Figure 9. Details along the cut ④ (a) the data lines of Q versus b for different system sizes. (b) with $L_{max} = 256$, the fitted y_t versus L_{min} and become stable at $L_{min} = 82$. Finite-size analysis of Eq. 13 yield reasonable values of the critical exponent, $y_t = \frac{1}{\nu} \approx 1.317(6)$. (c) data collapse of Q and (d) χ_{max} versus L in log-log plot.

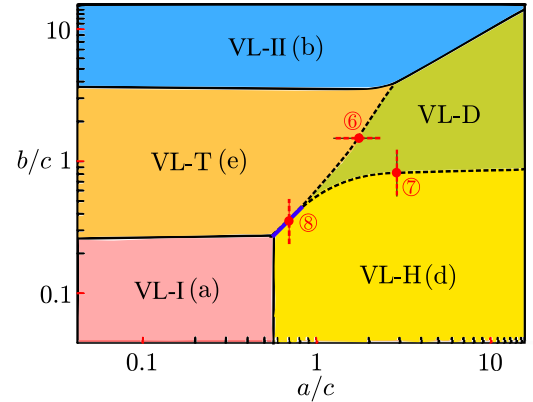


Figure 10. Phase diagram and four types of perfect vortex lattices. The lines are guides to the eye, and the points are obtained through finite-size scaling. For convenience, the labels (a)-(e) are used to mark the positions of the parameters taken for the snapshots drawn later in the phase diagram.

Figure 9 (a) shows the lines Q .vs. b in the regimes of b_c in the range $5.998 < b < 6.002$, with various system sizes from $L = 10 - 186$. The data for $L = 256$ has also been calculated, but it is not presented here as it closely resembles the data for $L = 186$. In Fig 9 (b), using the data Q .vs. b and the least squares method as given in Eq. 13, the critical weight parameter b and the critical exponent y_t are obtained, beginning with different values of $L_{min} = 10, \dots, 128$ and the fixed maximum size $L_{max} = 256$.

In Table I, when L_{min} is increased from 10 to 128, the estimated critical point remains stable around $b_c = 6$.

Additionally, the residual χ^2 per degree of freedom is close to 1, which is reasonably acceptable. Therefore, the final quoted value of b_c is taken as 6.000 09(9). In addition, taking into account that additional corrections might not be included in the fitting formula, we double the statistical fitting error in the final estimate $b_c = 6.000 0(2)$.

The fitting result for y_t becomes convergent when L_{\min} is increased to 82. By averaging the fitted y_t values for $L_{\min} = 82, 96, 128$, and using an error bar that is three times the standard deviation, our final result is $y_t = 1.317(6)$.

In Fig. 9 (c), based on the estimated results about b_c and y_t , data collapse is performed, where the horizontal axis represents $\frac{b-b_c}{b_c} L^{1/\nu}$ and the vertical axis represents Q , and the data from different lattice sizes overlap very well onto a single curve.

In Fig. 9 (d), using the relationship in Eq. 14, χ_{\max} vs L is plotted on a double logarithmic scale. The slope is obtained as $\frac{\gamma}{\nu} = 1.67(1)$. Using the estimated y_t , $\gamma = 1.26(1)$ is obtained. The error is calculated using the error propagation formula. For the exponent β , we use the scaling of the square root of magnetization defined in Eq. 7 as follows

$$M_{\text{rms}}^{b=b_c} \propto \sqrt{L^{2-d-\eta}} \propto L^{-\frac{\beta}{\nu}}, \quad (16)$$

where $d = 2$ is the dimension of space. The detailed derivation is shown in [53]. Using a fit, we get $\frac{\beta}{\nu} = 0.189(4)$, and finally, $\beta = 0.14(2)$ is obtained. We also determine $\alpha = 0.482(8)$ from Eq. 15a. Finally, the exponents $\alpha, \beta, \gamma, \eta$ are obtained.

4. Discussion of possible mechanisms

The reason for the Ising universality ($y_t = 1$ at $a = 0.3$) in the above phase transition can be understood through the Z_2 symmetry breaking mechanism. In Fig. 9 (b), the degeneracy of the configuration is 2. The energy of the configuration is the same when all arrows are flipped. However, the vortices in the triangle are either counterclockwise or clockwise, but the arrangement structure remains fixed. At the same time, swapping the positions of the counterclockwise and clockwise rotations results in the same energy; only the configuration of vertex $b2$ changes to vertex $b1$, and therefore the system exhibits Z_2 symmetry breaking. As b decreases, when the system moves from the VL-II (b) phase and enters the VL-T phase (e), as shown in Fig. 11 (e), the arrangement of counterclockwise and clockwise rotations becomes disordered. The system then exhibits Z_2 symmetry.

When $a = 5$ and $y_t = 1.317(6)$, the phase transition from the VL-II(b) phase to the VL-D phase does not belong to the Ising class, which is understandable.

At this parameter point, since both a and b are much larger than 1, the system tends to favor the striped region. The direction of the arrows only breaks the sym-

metry in the x direction, and it is not a perfect ordered-disordered phase transition. In the direction perpendicular to x -direction, no symmetry breaking occurs and it remains random. Therefore, it cannot be called a Z_2 symmetry-breaking mechanism.

From the perspective of vortices, when the phase changes from the VL-II(b) phase to the VL-D phase, the vortices on the triangular faces are directly annihilated, rather than swapping the vortices. This may be a new type of phase transition induced by topological excitations or topological annihilation, with a critical exponent of $y_t = 1.317(6)$.

B. Phase diagram by vortex

1. vortex lattice phases

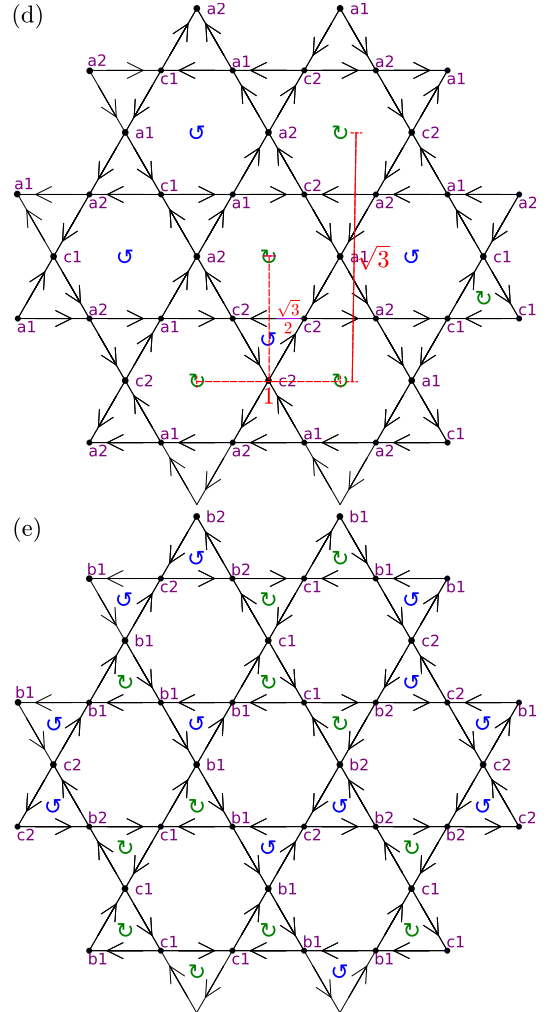


Figure 11. Snapshots of the (d) VL-H and (e) VL-T phases.

In Fig. 10, the phase diagram is shown by vortex-related quantities. The phase diagram includes various VL phases. The VL phases are classified as the VL-I

Table I. Fitting results for the Binder ratio Q using the ansatz Eq. (13).

Obs.	L_{min}	χ^2/DF	b_c	y_t	Q_0	e_1	e_2	f_1	ω
Q	10	8.0412784152	6.000 07(1)	1.376(2)	0.5495(1)	0.115(1)	0.0136(5)	0.017(2)	1
	16	3.3905907513	6.000 06(1)	1.374(2)	0.5471(1)	0.116(1)	0.0152(5)	0.105(4)	1
	32	3.0189990861	6.000 06(1)	1.369(2)	0.5469(3)	0.119(1)	0.0159(5)	0.11(1)	1
	48	2.6083228630	6.000 06(2)	1.361(3)	0.5475(4)	0.123(1)	0.0169(6)	0.07(2)	1
	56	2.4206931032	6.000 06(2)	1.352(3)	0.5478(5)	0.129(2)	0.0184(7)	0.06(3)	1
	64	2.1953299937	6.000 07(3)	1.339(4)	0.5484(7)	0.138(2)	0.021(1)	0.01(4)	1
	82	1.6517468039	6.000 07(4)	1.320(5)	0.548(1)	0.152(3)	0.025(1)	0.01(8)	1
	96	1.7174687795	6.000 07(4)	1.317(7)	0.549(1)	0.155(4)	0.026(1)	-0.1(1)	1
	128	1.6734930484	6.000 09(9)	1.315(9)	0.556(3)	0.158(7)	0.027(2)	-0.7(3)	1

phase, VL-II phase, VL-T phase, VL-H phase, and VL-D phase.

For the first type of VL phase, marked by VL-I phase, the snapshot is shown in Fig. 7 (a). Regardless of whether the triangles are upright or inverted, the vortices rotate counterclockwise. In hexagonal faces, the vortices rotate clockwise. The winding number is $k = 1$ in both cases, indicating a perfect vortex lattice phase. This phase has been found experimentally in Ref. [20], and called “Ferrotoroidicity”.

For the second type of VL phases, marked by the VL-II phase, the snapshot is shown in Fig. 7 (b). Adjacent triangular faces have positive vortices with a winding number of 1, but they rotate in opposite directions. In contrast, in the hexagonal unit cell, the vortices are antivortices with a negative winding number of -2. The circles inside the honeycomb face represent the vortices formed by the arrows on the six edges, with a winding number of -2. Although the same vortex configuration has been observed in Ref. [54], we are the first to discover this phase in the 6V model.

For the third type of VL phase, marked by the VL-H phase, the snapshot is shown in Fig. 11 (d). The VL phase is a partial VL order, as vortices are present only in the honeycomb cells, while the triangular cells contain no vortices. In each unit-cell, the ratio of the a -type to the c -type is 2:1.

For the fourth type of VL phase, marked by the VL-T phase, the snapshot is shown in Fig. 11 (e). The VL-T phase is also a partial VL order, as vortices are present only in the triangular faces, while the honeycomb faces contain no vortices. This configuration also exists in the frustrated Kagome XY antiferromagnet [55].

2. BKT transitions

Due to the presence of vortices in the system, it is necessary to explore whether a BKT transition exists. Therefore, to detect such transition, it is necessary to define the vortex density as follows

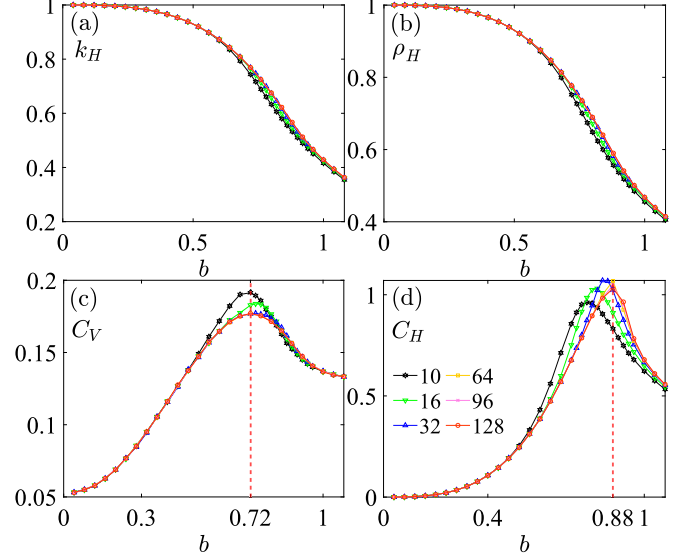


Figure 12. Details of the quantities along the cut ⑦: (a) the winding number density k_H , (b) vortex density ρ_H , (c) specific heat C_V , and (d) a specific heat-like quantity C_H . The convergence of the specific heat indicates the BKT transition.

$$\rho_H = \frac{1}{N_H} \sum_{i=1}^{N_H} n_i, \quad (17a)$$

$$\rho_T = \frac{1}{N_T} \sum_{i=1}^{N_T} n_i, \quad (17b)$$

where $N_H(N_T)$ denotes the total number of honeycomb(triangles) faces, $n_i = 1$ when vortices are present, and $n_i = 0$ if they are absent. The definition of the vortex density ρ_T for the triangular faces is similar. We also define quantities similar to the specific heat in order to determine the transition point of the BKT transition, as following,

$$C_H = \frac{N_H}{T^2} \left(\langle \rho_H^2 \rangle - \langle \rho_H \rangle^2 \right), \quad (18a)$$

$$C_T = \frac{N_T}{T^2} \left(\langle \rho_T^2 \rangle - \langle \rho_T \rangle^2 \right). \quad (18b)$$

In Figs. 12 (a) and (b), the winding number density k_H and vortex number density ρ_H are plotted as functions of b for a fixed value of $a = 2.5$ along the cut ⑦ in Fig. 10. Both quantities decrease as b increases. When b is small, the system resides in the perfect vortex lattice phase, i.e., the VL-H phase, and eventually melts into the disordered phase as b increases.

The type of phase transition can be identified by the signature of the specific heat C_V . In a BKT phase transition, the specific heat C typically does not show a singularity as the system approaches the critical region. As the size L increases, the peak of the specific heat converges. In Figs. 12 (c) and (d), both the specific heat C_V and the quantity C_H are plotted, and both converge as L approaches 96 and 128. In addition, along the cut ⑥, the results is also the BKT transition and the plots are not shown here in Fig. 10.

3. The new universality $y_t = 1.340(3)$ between the phases VL-H and VL-T

We have also discovered that a phase transition can occur between the two vortex phases, i.e., the VL-T and VL-H phases, along the cut ⑧ as shown in Fig. 10. After attempting, unlike the Ising model's order-disorder phase transition, we could not find a good Binder ratio of vortex density and energy to determine the phase transition point.

The critical exponent y_t can be fitted using the following finite-size scaling formula [56]:

$$C_V(L) = C_0 + L^{2y_t-d}(m + nL^{y_1}), \quad (19)$$

where $C_V(L)$ is the specific-heat to be fitted, L is the system size, C_0 , m , and n are constants, and d is the spatial dimension.

In Fig. 13 (a), it contains the raw data of specific heat C_V . Fortunately, as the size increases from $L=16$ to 216, the height of the specific heat peak increase sharper. It is to extrapolate the phase transition point at the thermodynamic limit by using the peaks corresponding to the their positions $b_c(L)$ of these finite sizes. The critical point $b_c(\infty)=0.3603(2)$ is obtained by this extrapolation method.

Then, using the values of $C_V(L)$ at the critical point $b_c(L \rightarrow \infty)$ and fitting the data according to Eq. 19, the following values are obtained: $2y_t - d = 0.681(5)$, $m = 0.030(9)$, and $C_0 = 0.230(4)$. In Fig 13 (b), plotting The data points of these two quantities $\frac{C_V^{b_c} - C_0}{m}$ versus L fit the linear behavior very well in log-log plotting. The conclusion is that the new exponent $y_t = 1.340(3)$ is obtained.

Actually, there is another method of get the exponent y_t . Using the scaling relationship [52],

$$\left| \frac{b_{\max}(L) - b_c(\infty)}{b_c(\infty)} \right| \sim L^{-y_t}, \quad (20)$$

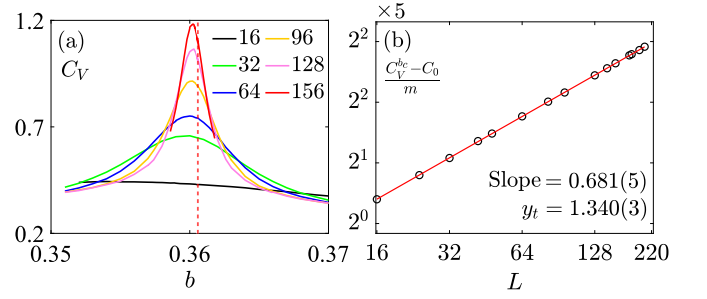


Figure 13. Finite size scaling of specific heat (a) The raw data of C_V as a function of b for system sizes $L = 16$ to $L = 156$. (b) The data of $\frac{|C_V^{b_c} - C_0|}{m}$ versus L presented in a log-log plot.

the exponent y_t can also be obtained. From the example in this paper, distinguishing a reliable $b_c(L)$ near the phase transition point (within the range of the fifth decimal place) requires a significant amount of computational effort. Therefore, the results are not shown here. We leave this task to be completed in the future.

4. vortex structural factors

In Ref. [20], the spin and vortex structural factors, defined on the triangular faces, were visualized. As the distances between the magnetic rods increase, which is equivalent to raising the temperature, the peaks of the structural factor gradually disappear, as expected.

Here, taking the snapshot in Fig 11 (d) as an example, we define the structure factor of vortex on the honeycomb faces as follows

$$S(q) = \frac{1}{N_c} \sum_{i,j}^{N_c} e^{iq \cdot (r_i - r_j)} \langle k_i k_j \rangle, \quad (21)$$

where N_c is number of honeycomb faces. For simplicity, the distance between the nearest neighboring honeycomb face be 1. r_i and r_j are the true coordinates of the vortex, k_i and k_j is the value of the number of vortex windings. In Fig. 14, the results of $S(q)$ for a lattice with $L = 16$ are shown. Fixing $a = 2.5$ and gradually increasing b from $b = 0.1$ to $b = 0.7$, $b = 1.1$, and $b = 1.7$, the peaks progressively darken. This behavior is consistent with the results shown in Fig. 12(a), where k_H decreases as b increases.

The location of one of the highlights appears in $(q_x, q_y) = (2\pi, \frac{2\sqrt{3}}{3}\pi)$. This is due to the fact that the distance between the vortices satisfies the following relationship:

$$\begin{aligned} \Delta x &= x_i - x_j = 1, \\ \Delta y &= y_i - y_j = \sqrt{3}, \\ q_{x(y)} &= \frac{2\pi}{\Delta x(y)}, \end{aligned} \quad (22)$$

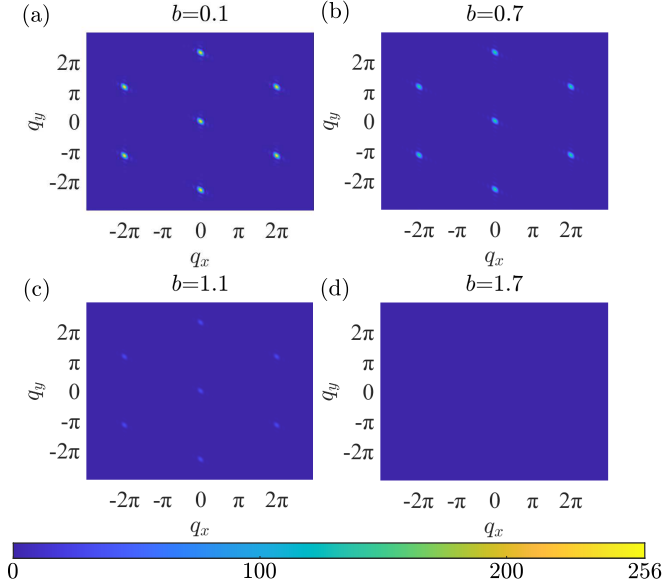


Figure 14. Schematic representation of the structure factors measured for different values of b when $a = 2.5$.

where the $\triangle x$ and $\triangle y$ are marked in red line segments in Fig. 11.

5. No fractional vortex phase

Here, we further analyze the four phases from the perspective of vortex excitation. Following [55], the topological charge q in a hexagon is defined as the average value of k_i the six connected triangular faces, as follows

$$q = \frac{1}{6} \sum_i k_i^T. \quad (23)$$

Different from the pure XY model on the Kagome lattice, the arrows of the six vertex model on the triangular edges can not form vortex with negative $k_i^T < 0$. This can be confirmed by exhaustively examining the 8 possible states $(+, \dots, -)$ of arrows on the three sides of a triangle. Both the clockwise and counterclockwise vortex correspond to positive $k_i^T > 0$ or $k_i^T = 0$ for other types of vertex configurations.

Therefore, in our perfect snapshots, as shown in Figs. 7 (a)-(b) and Fig. 11 (e), the vortex excitation defined in Eq. 23 is the integer $q = 1$ rather than a fraction such as $2/3$ or $1/3$ in Refs. [54, 55] for the XY model.

In addition, on the honeycomb faces, by enumerating all possible configurations, the vortex winding numbers are $k_H = -2, -1, 0, 1$, and there is no case for $+2$, still different from the pure XY model on the Kagome lattice.

IV. DISCUSSION AND CONCLUSION

In this work, we systematically investigated the vortex lattice phases and exponents in Kagome ice using the directed-loop Monte Carlo method. By simulating the theoretical six-vertex model on the Kagome lattice, we identified that the phase diagram is asymmetric with respect to $a = b$, unlike the square lattice, which is symmetric along $a = b$.

Four distinct VL phases are found. In comparison to the phases in [20], in our phase diagram, the VL-I phase corresponds to “Ferrotoroidicity” and the VL-T phase can be considered analogous to what is described as “Paratoroidicity”, where the vortex density is zero in hexagonal faces and one in triangular faces. However, the other two VL phases and detailed simulations are not reported in Ref. [20]. Our findings reveal that the various types of transitions between the phases. They are the BKT transition, Ising type, new universality classes $y_t = 1.317(6)$ and $y_t = 1.340(3)$. These results have not been reported before. Due to the difficulty in finding an order parameter similar to the Ising model’s order-disorder phase transition, the phase transitions between the VL-T and VL-H phases may be related with the Landau-incompatible transitions [57].

Despite these achievements, our work also has room for improvement. First, numerically, the directed loop Monte Carlo method, while effective, may have limitations in exploring more complex models, such as 16-vertex model or disorder vertex model,. Advanced computational techniques such as tensor network Monte Carlo [58, 59] may be required to extend our work. Second, experimentally, the vertex energy can be directly adjusted in the experiment by altering the positions of the magnetic rods, resulting in 16 different types of vertices [20]. However, it remains unclear whether the experiment can restrict the vertex types to the 6V subspace [20], as suggested by the theoretical model. Our results provide insights into potential realizations in water ice [7, 8], colloidal particle-based ice systems [5], colloidal active fluids in microchannel networks [17, 18].

In summary, our current work contributes to the advancement of numerical methods and experimental techniques to explore interesting phase-transition phenomena in Kagome lattice ice.

Acknowledgments This work was supported by the Hefei National Research Center for Physical Sciences at the Microscale (KF2021002), and the Shanxi Province Science Foundation with Grants No: 202303021221029 (W.Z.) and No:202103021224051 (J. Z.); C. D. is supported by the National Science Foundation of China (NSFC) under Grant Number 11975024; Y. J. was supported by the National Natural Science Foundation of China (Grant No. 12275263) and the Natural Science Foundation of Fujian Province of China (Grant No. 2023J02032).

Appendix A: Confirm of our code by enumeration

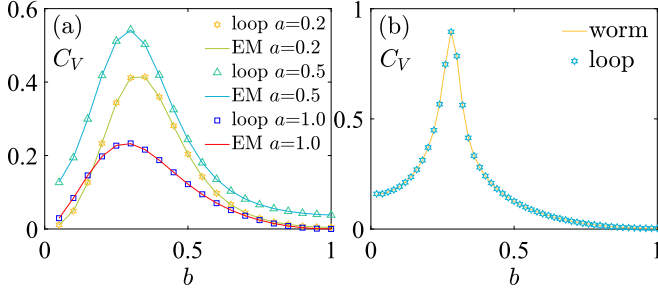


Figure 15. Comparison of C_V on the 2×2 Kagome lattice using the EM and MC methods. (b) With $a = 0.5$ and $L = 10$, the specific heat are measured by the worm and loop algorithms and the results are consistent.

To ensure the correctness of the code, the results of the directed loop algorithm are compared with those of the enumeration (EM) or brute-force method before the large-scale simulation. A 2×2 Kagome lattice is calculated, with 12 vertices ($2 \times 2 \times 3 = 12$) and 24 edges. The results for three different values of $a = 0.2, 0.5$, and 1 are computed while scanning b . The results obtained from both methods are the same, as shown in Fig. 15.

Appendix B: Worm algorithm

The following provides the worm algorithm and some results, which are also used to verify the results of the directed loop algorithm.

1. Pick a random site u in the Kagome lattice and randomly select one of its neighbors, denoted as v . The spin (or arrows) between u and v is flipped with a certain probability p_{acc} , and as a result, a pair of defects may appear in the Green function space G . Two types of defects are introduced: “three in and one out” and “three out and one in” with the weight of these vertices given by d . The acceptance probability can be

$$p_{acc} = \frac{w(u')w(v')}{w(u)w(v)}, \quad (B1)$$

where $w(u')$ and $w(v')$ are the probabilities of the type of vertex after flipping the spins. If it is rejected the round ends, if it is accepted, it enters the G -space and there is $(I, M) = (u, v)$ or (v, u) .

2. Randomly pick a neighbor of I called I' , try to flip the spin between I and I' , if after flipping, there is an undefined vertex then $p_{acc}=0$, otherwise the probability is p_{acc} defined in Eq. B1. If rejected, repeat the second step, if accepted, move I to I' , if I' is M , this round of updating ends, otherwise repeat step 2.

-
- [1] C. G. Salzmann, J. S. Loveday, A. Rosu-Finsen, and C. L. Bull, Structure and nature of ice XIX, *Nat. Commun.* **12**, 3162 (2021).
 - [2] S. T. Bramwell and M. J. P. Gingras, Spin Ice State in Frustrated Magnetic Pyrochlore Materials, *Science* **294**, 1495 (2001).
 - [3] S. H. Skjrv, C. H. Marrows, R. L. Stamps, and L. J. Heyderman, Advances in artificial spin ice, *Nat. Rev. Phys.* **2**, 13 (2020).
 - [4] C. Nisoli, R. Moessner, and P. Schiffer, Colloquium: Artificial spin ice: Designing and imaging magnetic frustration, *Rev. Mod. Phys.* **85**, 1473 (2013).
 - [5] A. Ortiz-Ambriz, C. Nisoli, C. Reichhardt, C. J. O. Reichhardt, and P. Tierno, Colloquium: Ice rule and emergent frustration in particle ice and beyond, *Rev. Mod. Phys.* **91**, 041003 (2019).
 - [6] L. C. Pauling, The Structure and Entropy of Ice and of Other Crystals with Some Randomness of Atomic Arrangement, *J. Am. Chem. Soc.* **57**, 2680 (1935).
 - [7] R. Ma, D. Cao, C. Zhu, Y. Tian, J. Peng, J. Guo, J. Chen, X.-Z. Li, J. S. Francisco, X. C. Zeng, L.-M. Xu, E.-G. Wang, and Y. Jiang, Atomic imaging of the edge structure and growth of a two-dimensional hexagonal ice, *Nature* **577**, 60 (2020).
 - [8] J. Hong, Y. Tian, T. Liang, X. Liu, Y. Song, D. Guan, Z. Yan, J. Guo, B. Tang, D. Cao, J. Guo, J. Chen, D. Pan, L.-M. Xu, E.-G. Wang, and Y. Jiang, Imaging surface structure and premelting of ice ih with atomic resolution, *Nature* **630**, 375 (2024).
 - [9] W.-C. Yue, Z. Yuan, Y.-Y. Lyu, S. Dong, J. Zhou, Z.-L. Xiao, L. He, X. Tu, Y. Dong, H. Wang, W. Xu, L. Kang, P. Wu, C. Nisoli, W.-K. Kwok, and Y.-L. Wang, Crystallizing kagome artificial spin ice, *Phys. Rev. Lett.* **129**, 057202 (2022).
 - [10] R. F. Wang, C. Nisoli, R. S. Freitas, J. Li, W. McConville, B. J. Cooley, M. S. Lund, N. Samarth, C. Leighton, V. H. Crespi, and P. Schiffer, Artificial ‘spin ice’ in a geometrically frustrated lattice of nanoscale ferromagnetic islands, *Nature* **439**, 303 (2006).
 - [11] A. D. King, C. Nisoli, E. D. Dahl, G. Poulin-Lamarre, and A. Lopez-Bezanilla, Qubit spin ice, *Science* **373**, 576 (2021).
 - [12] A. Libál, C. Reichhardt, and C. J. O. Reichhardt, Realizing Colloidal Artificial Ice on Arrays of Optical Traps, *Phys. Rev. Lett.* **97**, 228302 (2006).
 - [13] G.-W. Chern, C. Reichhardt, and C. J. Olson Reichhardt, Frustrated colloidal ordering and fully packed loops in arrays of optical traps, *Phys. Rev. E* **87**, 062305 (2013).
 - [14] C. Nisoli, Dumping topological charges on neighbors: ice manifolds for colloids and vortices, *New J. Phys.* **16**,

- 113049 (2014).
- [15] F. Ma, C. Reichhardt, W. Gan, C. J. O. Reichhardt, and W. S. Lew, Emergent geometric frustration of artificial magnetic skyrmion crystals, *Phys. Rev. B* **94**, 144405 (2016).
 - [16] C. J. Olson Reichhardt, A. Libál, and C. Reichhardt, Multi-step ordering in kagome and square artificial spin ice, *New J. Phys.* **14**, 025006 (2012).
 - [17] C. Jorge and D. Bartolo, Active-hydraulic flows solve the 6-vertex model (and vice versa), *arXiv preprint* (2024), [arXiv:2410.13377 \[cond-mat.soft\]](#).
 - [18] C. Jorge, A. Chardac, A. Poncet, and D. Bartolo, Active hydraulics laws from frustration principles, *Nature Physics* **20**, 303 (2024).
 - [19] Y. Tabata, H. Kadowaki, K. Matsuhira, Z. Hiroi, N. Aso, E. Ressouche, and B. Fåk, Kagomé ice state in the dipolar spin ice $\text{Dy}_2\text{Ti}_2\text{O}_7$, *Phys. Rev. Lett.* **97**, 257205 (2006).
 - [20] W.-C. Yue, Z. Yuan, P. Huang, Y. Sun, T. Gao, Y.-Y. Lyu, X. Tu, S. Dong, L. He, Y. Dong, X. Cao, L. Kang, H. Wang, P. Wu, C. Nisoli, and Y.-L. Wang, Toroidic phase transitions in a direct-kagome artificial spin ice, *Nat. Nanotechnol.* **19**, 1101 (2024).
 - [21] M. L. Latimer, G. R. Berdiyorov, Z. L. Xiao, F. M. Peeters, and W. K. Kwok, Realization of artificial ice systems for magnetic vortices in a superconducting moiré thin film with patterned nanostructures, *Phys. Rev. Lett.* **111**, 067001 (2013).
 - [22] V. K. Vlasko-Vlasov, J. R. Clem, A. E. Koshelev, U. Welp, and W. K. Kwok, Stripe Domains and First-Order Phase Transition in the Vortex Matter of Anisotropic High-Temperature Superconductors, *Phys. Rev. Lett.* **112**, 157001 (2014).
 - [23] B. Maiorov, G. Nieva, and E. Osquiguil, First-order phase transition of the vortex lattice in twinned $\text{YBa}_2\text{Cu}_3\text{O}_7$ single crystals in tilted magnetic fields, *Phys. Rev. B* **61**, 12427 (2000).
 - [24] E. Zeldov, D. Majer, M. Konczykowski, V. B. Geshkenbein, V. M. Vinokur, and H. Shtrikman, Thermodynamic observation of first-order vortex-lattice melting transition in $\text{Bi}_2\text{Sr}_2\text{CaCu}_2\text{O}_8$, *Nature* **375**, 373 (1995).
 - [25] T. Sasagawa, K. Kishio, Y. Togawa, J. Shimoyama, and K. Kitazawa, First-order vortex-lattice phase transition in $(\text{La}_{1-x}\text{Sr}_x)_2\text{CuO}_4$ single crystals: Universal scaling of the transition lines in high-temperature superconductors, *Phys. Rev. Lett.* **80**, 4297 (1998).
 - [26] M. Weigel and W. Janke, The square-lattice F model revisited: a loop-cluster update scaling study, *J. Phys. A: Math. Gen.* **38**, 7067 (2005).
 - [27] J. M. Kosterlitz and D. J. Thouless, Long range order and metastability in two dimensional solids and superfluids. (Application of dislocation theory), *J. Phys. C: Solid State Phys.* **5**, L124 (1972).
 - [28] J. M. Kosterlitz, Nobel Lecture: Topological defects and phase transitions, *Rev. Mod. Phys.* **89**, 040501 (2017).
 - [29] O. F. Syljuåsen and M. B. Zvonarev, Directed-loop Monte Carlo simulations of vertex models, *Phys. Rev. E* **70**, 016118 (2004).
 - [30] A. W. Sandvik, The Directed-Loop Algorithm, in *AIP Conf. Proc.* (AIP, 2003).
 - [31] O. F. Syljuåsen and A. W. Sandvik, Quantum Monte Carlo with directed loops, *Phys. Rev. E* **66**, 046701 (2002).
 - [32] O. F. Syljuåsen, Directed loop updates for quantum lattice models, *Phys. Rev. E* **67**, 046701 (2003).
 - [33] L. Pauling, The structure and entropy of ice and of other crystals with some randomness of atomic arrangement, *J. Am. Chem. Soc.* **57**, 2680 (1935).
 - [34] E. H. Lieb, Residual entropy of square ice, *Phys. Rev.* **162**, 162 (1967).
 - [35] M. A. Moore, Exactly solved models in statistical mechanics, *Physics Bulletin* **34**, 167 (1983).
 - [36] R. N. Onody and V. Kurak, Equivalences between a dimer, a vertex, and a spin model, *Phys. Rev. B* **38**, 5061 (1988).
 - [37] F. Y. Wu, The Potts model, *Rev. Mod. Phys.* **54**, 235 (1982).
 - [38] A. Glazman and R. Peled, On the transition between the disordered and antiferroelectric phases of the 6-vertex model, *Electron. J. Probab.* **28**, 1 (2023).
 - [39] H. Duminil-Copin, M. Gagnebin, M. Harel, I. Manolescu, and V. Tassion, The Bethe ansatz for the six-vertex and XXZ models: An exposition, *Probab. Surv.* **15**, 102 (2018).
 - [40] R. J. Baxter, *Exactly Solved Models in Statistical Mechanics* (Academic Press, London, 1982).
 - [41] N. Reshetikhin, *Lectures on the integrability of the 6-vertex model* (2010), [arXiv:1010.5031 \[math-ph\]](#).
 - [42] R. J. Baxter, H. N. V. Temperley, and S. E. Ashley, Triangular potts model at its transition temperature, and related models, *Proc. R. Soc. Lond. A* **358**, 535 (1978).
 - [43] B. Nienhuis, Exact critical point and critical exponents of $O(n)$ models in two dimensions, *Phys. Rev. Lett.* **49**, 1062 (1982).
 - [44] K. Koga, X. C. Zeng, and H. Tanaka, Freezing of confined water: A bilayer ice phase in hydrophobic nanopores, *Phys. Rev. Lett.* **79**, 5262 (1997).
 - [45] T. Zhong, H. Ma, P. Zheng, J. Zhang, and W. Zhang, First-order vortex lattice melting in bilayer ice: A monte carlo method study, *Phys. Rev. B* **109**, 224426 (2024).
 - [46] N. Prokof'ev, B. Svistunov, and I. Tupitsyn, "Worm" algorithm in quantum Monte Carlo simulations, *Physics Letters A* **238**, 253 (1998).
 - [47] N. Prokof'ev and B. Svistunov, Worm Algorithms for Classical Statistical Models, *Phys. Rev. Lett.* **87**, 160601 (2001).
 - [48] Y. Deng, T. M. Garoni, and A. D. Sokal, Dynamic critical behavior of the worm algorithm for the ising model, *Phys. Rev. Lett.* **99**, 110601 (2007).
 - [49] B.-Z. Wang, P. Hou, C.-J. Huang, and Y. Deng, Percolation of the two-dimensional XY model in the flow representation, *Phys. Rev. E* **103**, 062131 (2021).
 - [50] H. Chen, P. Hou, S. Fang, and Y. Deng, Monte Carlo study of duality and the Berezinskii-Kosterlitz-Thouless phase transitions of the two-dimensional q -state clock model in flow representations, *Phys. Rev. E* **106**, 024106 (2022).
 - [51] L. Zhang, M. Michel, E. M. Elçi, and Y. Deng, Loop-Cluster Coupling and Algorithm for Classical Statistical Models, *Phys. Rev. Lett.* **125**, 200603 (2020).
 - [52] A. W. Sandvik, *AIP Conference Proceedings*, Vol. 1297 (AIP Publishing, 2010) pp. 135–338.
 - [53] K. Rummukainen, *Phase transitions and finite size scaling* (2019), accessed on September 14, 2019.
 - [54] T.-Y. Lin, F.-F. Song, and G.-M. Zhang, Theory of the charge-6e condensed phase in kagome-lattice superconductors, *Phys. Rev. B* **111**, 054508 (2025).
 - [55] F.-F. Song and G.-M. Zhang, Phase coherence of charge-6e superconductors with a frustrated kagome xy antifer-

- romagnet, [Chin. Phys. Lett.](#) **42**, 037401 (2025).
- [56] M. N. Barber, R. B. Pearson, D. Toussaint, and J. L. Richardson, Finite-size scaling in the three-dimensional ising model, [Phys. Rev. B](#) **32**, 1720 (1985).
- [57] A. Prakash and N. G. Jones, Classical origins of landau-incompatible transitions, *Physical Review Letters* **134**, [10.1103/physrevlett.134.097103](#) (2025).
- [58] M. Frías-Pérez, M. Mariën, D. P. García, M. C. Bañuls, and S. Iblisdir, Collective Monte Carlo updates through tensor network renormalization, [SciPost Phys.](#) **14**, 123 (2023).
- [59] T. Chen, E. Guo, W. Zhang, P. Zhang, and Y. Deng, Tensor network Monte Carlo simulations for the two-dimensional random-bond ising model, [Phys. Rev. B](#) **111**, 094201 (2025).